

# Molecular Dynamics Study of the Formation of Porous Films by Room-Temperature Physical Vapor Deposition of Silica

Nikita S. Shcheblanov, Céline Léonard, Quy-Dong To, Mikhail E. Povarnitsyn, and Anaël Lemaître\*

 Cite This: *J. Phys. Chem. C* 2024, 128, 17606–17618

 Read Online

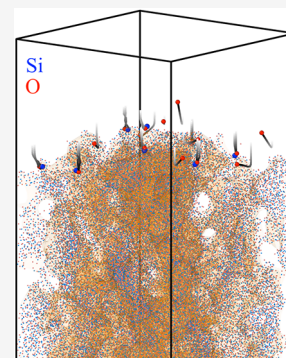
ACCESS |

 Metrics & More

 Article Recommendations

 Supporting Information

**ABSTRACT:** Low-temperature physical vapor deposition is studied by means of molecular dynamics (MD) simulations using the reactive force field (ReaxFF) potential. In contrast with prior MD studies of this process, which employed nonreactive, rigid ion force fields, our approach allows for accurate modeling of the reactive incorporation of impinging particles, generated by the vaporization process, into the growing film. The use of the ReaxFF also enables us to properly model the charges of impinging particles and their electrostatic interactions with the atoms, forming the topmost layers of the growing film. In order to better evidence the associated effects, we focus on the conditions of growth when the impinging particles have moderate kinetic energies (below a couple of electronvolts). We thus evidence that under these conditions, impacting particles tend to be strongly deflected during the last stages of their approach to the film, and all the more so when they are slow. As a result, they tend to be captured by denser regions, leading to the formation of porous microstructures. This phenomenon results from the polarization of Si–O bonds and the tendency of silicon atoms to surround themselves with oxygen atoms, leading to an overall polarization of the interface between dense matter and pores.



## INTRODUCTION

Physical vapor deposition (PVD) is a technique of primary importance for the production of amorphous coatings,<sup>1,2</sup> in particular amorphous oxides, which are key components in many advanced technologies in areas as diverse as biosciences, telecoms, energy production and storage, or gravitational wave detection. Deposition proceeds in a vacuum chamber via the sputtering of a source material by an ion or electron beam. The sputtered material travels through the chamber, where it may collide or react with residual gases, and impinges on a substrate, thus leading to the progressive growth of a film.

In low-*T* (room temperature) PVD, the coating temperature typically stays around or even below 100 °C, which is quite low compared with the characteristic energies of chemical bond formation for oxides (in the range of several electronvolts, or eV). Under such low-*T* conditions, atomic diffusion is inoperative, which guarantees that coatings develop an amorphous and isotropic microstructure, which is essential to achieving the desired optical, mechanical, or electrical properties. However, it entails that the deposited films are strongly out-of-equilibrium: in sharp contrast with usual glasses, they do not result from the quench of an equilibrated liquid, with the consequence that their microstructure and physical properties may strongly depend on the details of the deposition process.

A certain degree of simplification arises from the fact that growth results exclusively from the progressive incorporation of an incident flux of the material on the growing film. Therefore, the film microstructure and end properties are fully determined by the nature and kinetic energy of the particles (atoms, ions, molecules, and molecular ions) that constitute the plume

impinging on the substrate. However, experimentally accessing these parameters requires using an energy-resolved mass spectrometer that should be inserted at the location of the substrate into a deposition chamber. This is a difficult characterization, and we are not aware of any published data for the PVD of oxides, which leaves considerable uncertainty about the composition of the plume.<sup>3</sup> Theoretical models of sputtering exist,<sup>4–7</sup> but the process is quite complex and highly sensitive to the energy of the beam irradiating the target; moreover, the sputtered material may collide or react with residual gases in the chamber during flight time, which may significantly affect the plume composition and the kinetic energies of its constituents when they reach the growing film. Therefore, sputtering theories cannot be relied upon in the absence of direct experimental characterization of the impinging particles.

In such a context, MD simulations can provide invaluable inputs about the low-*T* growth process by making controlled assumptions about the deposited species and assessing their consequences on the end film properties. Growth simulations focus on a small surface element of the substrate and proceed by repeatedly introducing particles of chosen stoichiometry and

**Received:** April 3, 2024

**Revised:** August 18, 2024

**Accepted:** August 20, 2024

**Published:** September 30, 2024



kinetic energy above the growing film, thus simulating impact events iteratively. Early studies<sup>8–10</sup> were too limited by computer capabilities, however, to reach steady growth.

A main difficulty has been to numerically achieve steady growth of nearly stoichiometric films as observed in experiments. Taguchi and Hamaguchi<sup>9,10</sup> succeeded in doing so in a study of reactive sputtering, where an Si target is sputtered in the presence of an oxygen gas feed: they modeled this situation by introducing a strong excess of atomic oxygen and thus managed to produce stoichiometric films. However, nearly stoichiometric silica is routinely deposited by the sputtering of a silica target, without an oxygen gas feed.<sup>11–14</sup> Much of the recent activity on the topic has been produced by the group of Grigoriev and coworkers, who focused on simulations under such conditions,<sup>15–30</sup> but they encountered difficulties in producing stoichiometric and homogeneous films under normal incidence.

The issue is that oxygen has a much higher rebound probability than silicon on the growing film,<sup>3,9</sup> so that a stoichiometric influx tends to produce strongly oxygen-deficient films. Grigoriev mitigate this issue by keeping the rebounding oxygens in the numerical cell, which forces the whole system to remain stoichiometric but leads to the formation of a spurious atomic-oxygen-rich, high-density gas above the growing film. This artificial forcing of stoichiometry is likely the cause of difficulties these authors initially encountered in reaching steady growth.<sup>25</sup> They did recently achieve a steady growth regime,<sup>29</sup> but only beyond 20 nm, whereas uniformity is expected to be achieved after barely a few atomic layers.<sup>3</sup>

A recent study<sup>3</sup> managed to achieve steady growth of nearly stoichiometric films, without any noticeable transient, while constructing an algorithm in which the rebounding atoms or ions are properly eliminated from the simulation cell after every deposition event. These authors emphasized that e-beam deposition “permits the formation of nearly stoichiometric films without significant incorporation of residual molecular oxygen even at high partial pressures<sup>31</sup>”, while simulations and thermal evaporation experiments<sup>32</sup> show that significant fractions of atomic or molecular oxygen rebound. On this basis, they concluded that most of the vaporized oxygen atoms during e-beam sputtering should be bonded to silicon atoms and studied the deposition of SiO<sub>2</sub>. They found that this assumption led to the production of numerical (MD) films that are not only homogeneous but also jointly present several properties comparable with the experimental ones (namely density, stress, and stoichiometry), provided one assumes that the particles produced by e-beam vaporization impact the growing film with kinetic energies of the order of a few eV.

These advances open the route toward the construction of increasingly accurate and predictive MD simulations of the low-*T* PVD process. However, all existing studies have used nonreactive force fields, which do not properly take into account the bond-breaking and forming processes. This is unsatisfactory for modeling PVD growth since the process of incorporation of an impinging particle into the growing film involves changes in chemical bondings and charge transfers. An additional issue is that the nonreactive force fields used in former deposition simulations involved the so-called rigid-ion simplification, in which each atom carries a partial charge determined after fitting the model prediction with various material properties.<sup>33</sup> This might lead to an improper representation of the long-range interactions between impinging particles and the charge heterogeneities lying at the surface of the growing film. Indeed, the sputtering process is accompanied

by charge transfers,<sup>4–7</sup> so significant fractions of the impinging particles should be expected to be ionized.

Here, we address these key issues by designing a deposition algorithm based on ReaxFF,<sup>34,35</sup> one of the most versatile reactive force fields, which has proved its usefulness in various research areas of chemistry and physics of materials science<sup>35–41</sup> and was recently used to study ion implantation.<sup>42,43</sup> Since ReaxFF simulations have a significantly higher numerical cost than nonreactive force fields, it compels us to further optimize the algorithm of ref 3 by implementing minimization techniques to eliminate the excess energy introduced in the simulation cell by deposition events. As we will detail below, this is justified by the fact that impact events are quite separated in time and space and by the irrelevance of activated processes under low-*T* growth conditions. Since the ReaxFF represents correct charge transfers and charge distributions, this algorithm will also enable us to properly take into account the Coulombic interactions between the growing film surface and impinging particles.

The possibilities offered by the ReaxFF to properly model both chemical reactions and Coulombic effects motivate us to test our algorithm while focusing on growth conditions under which the incident particles have a low impact velocity.<sup>44,45</sup> Such conditions, indeed, can be realized via various deposition techniques and have been shown to favor the formation of porous films,<sup>46–50</sup> but the origin of these structures is not precisely known. We expect that Coulombic effects play a prominent role in pore formation because the slower the impinging particles, the more likely they are to be significantly deflected due to their interaction with surface charge heterogeneities before they actually enter into chemical bonding. Using the ReaxFF will enable us to document this idea and to produce reasonable porous structures that we will characterize. We will thus show that PVD may lead to the formation of highly porous films through which a probe of radius <6 Å may percolate.

## MODELS AND METHODS

**Modeling Assumptions.** Under usual physical vapor deposition conditions, the impacts of the sputtered species on the substrate are very separated from each other in time and space.<sup>3</sup> Indeed, for a silica film growing at the rate of a few Angstroms per second, each ~100 nm<sup>2</sup> surface element receives a silica atom every few milliseconds, while it takes just a few picoseconds for the incident atoms to form covalent bonds and become permanently embedded in the growing film microstructure during an impact.

Each impact introduces a slight excess of energy in the film due to the kinetic energy of the impinging particles and the energy released in the chemical bond formation. The large separation between impact events allows this energy to leak out from the film by thermal diffusion, which is why growth usually occurs at most around 100 °C.

This low temperature—compared to the binding energies—guarantees that there is no atomic diffusion between impacts. Therefore, it can be considered that, between impact events, atoms only fluctuate around an inherent state (i.e., a local minimum of the potential energy). Thus, in a deposition simulation, which necessarily focuses on a small surface element (of the order of a few nanometers on a side), it is not necessary to simulate the time intervals between two impacts. It suffices to simulate the series of impacts while ensuring that the energy gained by the system during impacts is properly drained out of the simulation cell.

It should be noted that, during an impact, some atoms of the incident species may bounce back and thus fail to insert themselves into the growing film, or some atoms initially present in the film may be torn off. In practice, these two types of atoms fly away from the substrate to the chamber walls, where they either adsorb or reenter the residual atmosphere. From the point of view of the simulation, these atoms must be eliminated.

**Deposition Algorithm.** A deposition simulation starts with the production of a small volume element of the substrate. For this purpose, in the NPT ensemble at pressure  $p = 0$ , we first melt a fully periodic MD model of silica at a high temperature (4000 K for a total of 1 ns), and then quench it at a rate of 1 K/ps down to 0 K. At the end of this process, the system is cubic, with a linear size of  $\approx 102$  Å and a density of 2.2 g/cm<sup>3</sup>. The boundary conditions along the  $z$ -axis are then released; a slab of 30 Å thickness along this axis is retained, and the dimension of the cell in the  $(x,y)$  plane is fixed from then on. We checked, consistently with ref 3, that the substrate has no measurable influence on the film growth under the studied conditions.

Following the modeling assumptions detailed above, deposition is performed via an iterative algorithm involving, at each step, the following series of operations:

1. A few incident ions or molecules of prescribed composition and kinetic energies are introduced into the cell above the substrate at an arbitrary position in the  $(x,y)$  plane. In order to minimize the simulation time, we take advantage of the fact that the interaction potential used (see below) has a finite cutoff, and place the incoming particles along the  $z$ -axis at a distance just beyond the interaction range with any atom of the surface. The exact number of introduced particles will be discussed later.
2. The impact and reaction of the impinging species are simulated in the NVE ensemble, since these are rapid processes during which energy has no time to diffuse away from the volume of the cell. In order to distinguish the initial flight of a molecule toward the substrate from reactive processes, an impact time is identified by detecting the instant when the  $z$ -component of the momentum of each molecule first changes its sign and becomes positive. We found that a typical duration of 2 ps is sufficient to determine the final configuration after the impact. This has been tested for each choice of parameters.
3. A partitioning algorithm is used to detect and eliminate the uncondensed particles (bounces and ejected material).
4. The energy introduced by the impact process is eliminated by performing a minimization of the entire system.
5. Since some atoms may be pushed away from the film during minimization, we return to step 3 and repeat steps 3, 4, and 5, as long as we identify atomic clusters that must be eliminated.

In ref 3 and in previous low- $T$  deposition simulations,<sup>29</sup> step 4 or its analogue was performed by carrying out a short simulation in the NVT ensemble at room temperature for a few picoseconds. This is enough to thermalize the system at the target temperature but entails a significant numerical cost. The optimization we propose rests upon the observation that the precise value of the target temperature is of little relevance, provided it is low enough compared with the binding energies

(typically several eV). Instead of thermalizing the film to the precise value at which growth proceeds, it is sufficient to guarantee that there is no unphysical increase in the temperature in the system. This leads us to propose an improvement of previous deposition algorithms by performing an energy minimization of the system at step 4: bringing the system toward the closest inherent state reduces the film temperature to a negligible value before the next impact. The minimization does not need to be highly accurate since its objective is not to access detailed properties of the locally stable minima but merely to avoid a spurious increase of heat inside the simulation cell. We use a convergence criterion of  $1.0 \times 10^{-10}$  for the relative energy difference between iterations and a force tolerance of  $1.0 \times 10^{-10}$  (kcal/mol)/Å, which are negligible compared with thermal fluctuations at room temperature. With this modification, the time required to simulate step 4 becomes negligible, which leads to a significant gain in simulation time. For comparison, indeed, in ref 3 thermalization required a 4 ps simulation, which is twice the simulated duration of impact, and hence would incur an extra simulation time of 200%. Similarly, Grigoriev uses a total of 6 ps<sup>23,29</sup> of simulation time per cycle. By using minimization, which takes a negligible simulation time, we essentially reduce the simulation time to 2 ps per cycle, which is quite a significant improvement.

**Interaction Potential.** The most commonly used force field potentials, like the BKS, TS, or COMB potentials,<sup>51–55</sup> are empirically determined to approximate the energy of the system as a function of atomic positions but do not accurately take into account the possibility for atoms to display different forms of connectivity due to the formation or opening of chemical bonds.

The Reactive Force Field (ReaxFF) is a bond-order-dependent potential, meaning that it introduces a notion of connectivity between atoms; the potential energy of the system thus consists of contributions from bond-order-dependent and nonbonded interactions (the latter being the van der Waals and Coulomb energies). The bond order is calculated based on the interatomic distances of all atom pairs at every iteration. Hence, the energy contributions from bond-order-dependent terms such as bond, valence angle, and torsion angle vanish upon bond dissociation, while leaving only the nonbonded interactions. Additionally, the electronegativity equalization method<sup>56</sup> is used to derive the atomic charges. This enables the ReaxFF to take into account both electrostatic interactions and chemical reactions occurring between atoms.

Tuning the ReaxFF for a specific system, however, remains a delicate issue and proceeds via the optimization of model parameters by comparison with experimental and quantum simulation data.<sup>34,38,39,57–59</sup> The resulting models were shown to properly predict an array of molecular structures,<sup>57,58,60</sup> and phenomena, especially for silicon-based materials, such as silicon sputtering,<sup>61,62</sup> high-temperature oxidation of silicon,<sup>63,64</sup> the reactive dynamics of silica with water, or the dynamics of confined water in clays; but it must be kept in mind that they may also inaccurately estimate the barriers associated with some reactions, as was shown for the dimerization of silica.<sup>65</sup> For this work, in the perspective of later enriching our deposition model to take into account the presence of water, we have used the parameter set of Pitman and van Duin,<sup>66</sup> which is based on the work by Fogarty et al.<sup>67</sup> for the Si/O subsystem of our interest.

All the MD simulations presented here use the LAMMPS<sup>68</sup> package and its ReaxFF implementation.<sup>57</sup> For steps 3 and 4, we use the partitioning algorithm and the Polak–Ribière minimization algorithm, respectively, included in LAMMPS.

**Pore and Microstructure Analyses.** We will characterize the produced films using a combination of observables and techniques:

- by determining mean properties (density, stoichiometry, and stress), either over the whole film, or averaged in the  $(x,y)$  plane and resolved along the  $z$ -axis to check film homogeneity;
- by measuring atomic coordination, while using the coordination provided by the ReaxFF to evidence the presence of defects;
- by characterizing the film porosity using a modified version of Zeo++<sup>69</sup> and OVITO<sup>70</sup> for visualization.

Zeo++<sup>69</sup> is an open-source software dedicated to the characterization of nanoporous materials, which can provide information about pore sizes and morphologies (pockets or channels). The software rests on the construction of a periodic Voronoi network around the atoms, which provides an efficient algorithmic way to identify the closest atom to every point in the system and hence to determine whether any point can be occupied by the center of a spherical probe of a given radius  $R$ . Combined with Dijkstra's algorithm,<sup>72</sup> it can identify connected sets of accessible points for a given spherical probe.

Since deposited configurations present significant fractions of coordination defects (i.e., oxygen or silicon atoms that are not 2- and 4-coordinated, respectively), we parametrized Zeo++ to take into account the dependence of atomic radii on the coordination number, as detailed in Table 1. We have also adapted Zeo++ to the presence of an open surface, so as to identify the main pore channel connected to the free surface, as detailed in the Supporting Information.

**Table 1. Atomic/Ionic Radii  $R_{CN}$  (Å) for Si and O As a Function of the Coordination Number (CN)<sup>a</sup>**

CN	$R_{CN}$ (O)	$R_{CN}$ (Si)
0	1.52	2.10
1	1.435	1.64
2	1.35	1.18
3	0.0	0.72
4	0.0	0.26
≥5	0.0	0.0

<sup>a</sup>Data are taken from ref 71.

## RESULTS AND DISCUSSION

The parameter space being overwhelmingly large, we will limit our study to three types of incoming particle fluxes and three values of their kinetic energies. The explored compositions of the incoming flux are (I) SiO<sub>2</sub> only; (II) SiO<sup>+</sup> and O<sup>-</sup>; (III) SiO<sub>3</sub><sup>-</sup> and SiO<sup>+</sup>. In the last two cases, both ions are introduced in equal numbers, which guarantees that the total incoming particle flux has the stoichiometry of SiO<sub>2</sub> and is essential to obtain a meaningful comparison with case (I). This set of fluxes enables us to address two issues. First, by comparing the case of neutral incoming particles (SiO<sub>2</sub>) with fluxes involving ionized ones, we will assess the role of Coulombic interactions in determining atomic rebound probabilities and thus the final stoichiometry of the films. Second, by comparing case (II) with the two others, we will assess the difficulty in incorporating atomic oxygen ions versus oxygen atoms that are already chemically bonded to silicon inside incoming particles.

As explained in our discussion of modeling assumptions, impact events are quite separated in space and time. Ideally, we would like to simulate each event separately, i.e., by introducing a single particle at step (1) of our algorithm. This, however, would be too numerically costly, and thus, we need to introduce several particles jointly at the beginning of each cycle. This is consistent if the number of introduced particles is small enough that they can be placed beyond the interaction range and do not engage in significant mutual interactions during impacts. After a few tests, we thus model fluxes (I), (II), and (III) by introducing at each cycle  $8 \times \text{SiO}_2$ ,  $8 \times (\text{SiO}^+ + \text{O}^-)$ , and  $4 \times (\text{SiO}_3^- + \text{SiO}^+)$ , respectively.

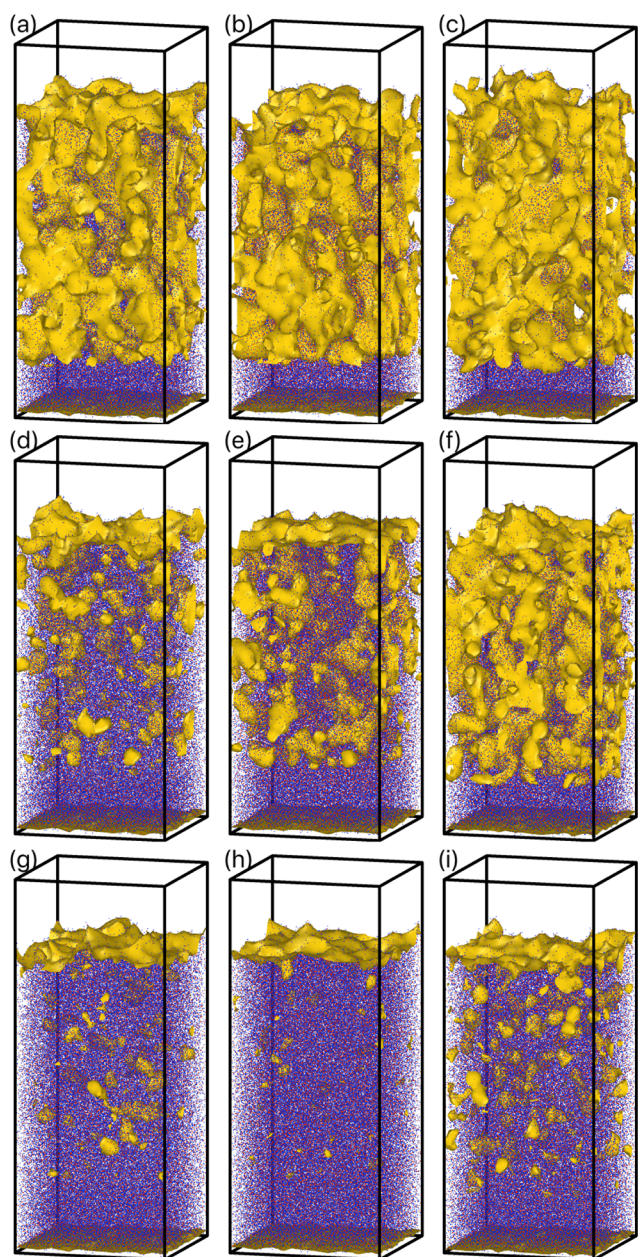
Three values of the kinetic energy of the impinging particles are studied:  $E = 0.25, 1.0, \text{ and } 2.0$  eV. They were chosen to allow us to investigate the mechanisms of growth of porous films at low impact velocities.<sup>3,44,45</sup> We assume for simplicity that all the considered incoming species have the same kinetic energies.

Figure 1 presents snapshots of the final configurations of the produced films after growth in all of the studied conditions. The pictures are organized with the incoming particle kinetic energy increasing from top to bottom, and the incoming fluxes (I), (II), and (III) from left to right. In these snapshots, the colors are chosen so that the oxygen and silicon atoms are shown in blue and red, respectively, and the free space in yellow. We immediately see that the films produced at the lowest  $E = 0.25$  eV are highly porous, that pores are still very visible and seem to be strongly interconnected at  $E = 1.0$  eV, whereas dense films with a few isolated pores are obtained at  $E = 2.0$  eV.

**Locally Averaged Properties.** From our films, we now extract an array of local properties as a function of  $z$  by virtually decomposing the film into horizontal slabs of thickness  $5 \text{ \AA}$ , over which we perform averages. We thus report in Figure 2, as a function of  $z$ , the local density ( $\rho$ ), the local stoichiometry ( $S$ , defined as the number of oxygen atoms per silicon atom), and the in-plane stress [ $\sigma \equiv (\sigma_{xx} + \sigma_{yy})/2$ ].

In all these plots, the substrate is located in the  $z < 0$  domain and the film in the  $z > 0$  one. Thus, our data clearly show that, under all of the explored conditions, the films develop homogeneous properties beyond a short transition region just above the substrate. For stoichiometry (Figure 2, top row), this transition is barely visible, i.e.,  $S$  achieves steady-state values beyond a few Ångströms. For local density (Figure 2, middle row), the extent of this transition region is visibly larger, and it is also sensitive to the kinetic energy of incoming particles,  $E$ : at  $E = 0.25$  eV, indeed, the transient of  $\rho$  extends over a nearly 20 nm region regardless of the incoming flux composition. This is presumably related to the formation of the large pores that are visible in Figure 1 and that we will characterize later. In contrast, this transition is barely visible at  $E = 1.0$  eV. Local stress (Figure 2, bottom row) should also be sensitive to the presence of pores, and indeed, a close examination of Figure 2g shows that it presents a weak transition comparable with that of  $\rho$ , for  $E = 0.25$  eV. It also seems that stress converges more rapidly to its steady-state values for higher values of  $E$ , but this is difficult to fully assert due to the significant fluctuations in this observable.

By averaging these data on the interval  $z \in [30,150] \text{ \AA}$ , we extract the mean values of the considered local properties, which we report in Figure 3 as a function of  $E$ , for each studied composition of the incoming particle flux. These plots demonstrate a strong influence of both  $E$  and the nature of the incoming particles. It is especially noteworthy in Figure 3a that the films produced by deposition of SiO<sub>2</sub> [case (I)] are nearly



**Figure 1.** Snapshots of the deposited films with the voids being highlighted. Oxygen and silicon atoms are shown in blue and red, respectively, and the free space in yellow. The upper row is for  $E = 0.25$  eV; the middle row is for  $E = 1.0$  eV; the lower row is for  $E = 2.0$  eV. Columns from left to right correspond to different deposition species:  $8(\text{SiO}_2)$ ,  $8(\text{SiO}^+ + \text{O}^-)$ , and  $4(\text{SiO}_3^- + \text{SiO}^+)$ . The size of all boxes is  $102 \times 102 \times 250$  Å. The densities of the deposited films are: (a) 1.19, (b) 1.33, (c) 1.08, (d) 1.72, (e) 1.93, (f) 1.5, (g) 1.87, (h) 2.24, and (i) 1.93  $\text{g}/\text{cm}^3$ .

stoichiometric regardless of  $E$ . In contrast, the films produced with either  $\text{SiO}^+ + \text{O}^-$  [case (II)] or  $\text{SiO}_3^- + \text{SiO}^+$  [case (III)] tend to be oxygen-deficient and increasingly so as the kinetic energy of incoming particles decreases.

Figure 3b shows that film density may achieve a very broad range of values, from about  $1.0 \text{ g}/\text{cm}^3$  at  $E = 0.25$  eV in case (III) to more than  $2.2 \text{ g}/\text{cm}^3$  at  $E = 2.0$  eV in case (II). These changes are consistent with our observations of porosity in the images of Figure 1. For each case, the trend is monotonic with the impact

kinetic energy in the studied range: higher  $E$  values lead to the formation of denser and less porous films.

In ref 3, which presented simulation data for the deposition of  $\text{SiO}_2$  particles and hence corresponds to case (I), albeit with a nonreactive potential, the in-plane stress was shown to be a nonmonotonic function of  $E$  with a maximum in the eV range where films become tensile. The data of Figure 3c, now obtained using the ReaxFF potential, confirm the possibility of forming tensile films at low  $E$ . The nonmonotonicity of the in-plane stress is also visible in case (II) by comparison of the  $E = 1.0$  and  $2.0$  eV films, but less so in cases (I) and (III). In these latter cases, although the stress tends to round off at the largest  $E$ , the nonmonotonicity is either too weak to be deemed significant [case (I)] or not visible at all [case (III)].

Due to the numerical cost of ReaxFF simulations, we could not accumulate data over a broader range of  $E$  values and explore whether the stress becomes compressive at higher  $E$  in these last two cases; but we presume this is the case since higher impact energies should produce denser and thus increasingly compressive films. In order to further support this idea, we plot in Figure 3d the in-plane stress versus the film density. All of our data seem to roughly follow a similar trend, with a maximum of (tensile) stress around a density of  $\approx 1.75 \text{ g}/\text{cm}^3$ . It is thus consistent that we could obtain significant compressive stress only in case (II),  $E = 2.0$  eV, which corresponds, by far, to our densest film. Our goal being to focus on low- $E$ , tensile, and porous films, the data of Figure 3c,d, on top of our qualitative observations of pores, support that we are exploring the right parameter range.

**Atomic Coordination Analysis.** Due to the strongly out-of-equilibrium character of low- $T$  deposition, the films obtained by this process are expected to comprise significant fractions of structural defects, all the more so that they depart from the ideal,  $S = 2$ , stoichiometry. This is confirmed by inspection of the mean densities of  $n$ -coordinated atoms (denoted below as Si- $n$  or O- $n$ ), which are averaged over the whole films<sup>4</sup> and reported in Figure 4. Considerable differences are observed with fused silica, in which oxygen and silicon atoms are predominantly two- and four-coordinated, respectively. Here, indeed, in all of our films, about half of the silicon atoms are three-coordinated. The fraction of Si-4 atoms is, at most, on the order of about 50%, but achieves rather small values in the most oxygen-deficient films, i.e., in cases (II) and (III) at  $E = 0.25$  and  $1.0$  eV. There is also a significant fraction of undercoordinated oxygen atoms (O-1), i.e., dangling bonds.

In complement to this discussion, several observables characterizing atomic bonding are presented in the Supporting Information: Si–O–Si and O–Si–O angles as well as Si–O bond lengths. These data confirm the high degree of statistical homogeneity of our films since all the measured observables become essentially  $z$ -independent beyond a small thickness, of the order of a nanometer above the substrate. However, they also present values that are markedly different from those of the thermally equilibrated glass we used to prepare the substrate, and are measurably dependent on growth conditions.

**Porosity Analysis.** We now turn to the key objective of the paper, i.e., the evidence and characterization of the porosity. Along this analysis, it is essential to bear in mind that, unlike, e.g., zeolites or materials consisting of macroscopic continuous phases surrounding empty space, there are no intrinsic (probe-independent) pores in discrete systems such as ours. A strictly pointwise probe would indeed systematically percolate throughout the material, without this feature carrying much physical

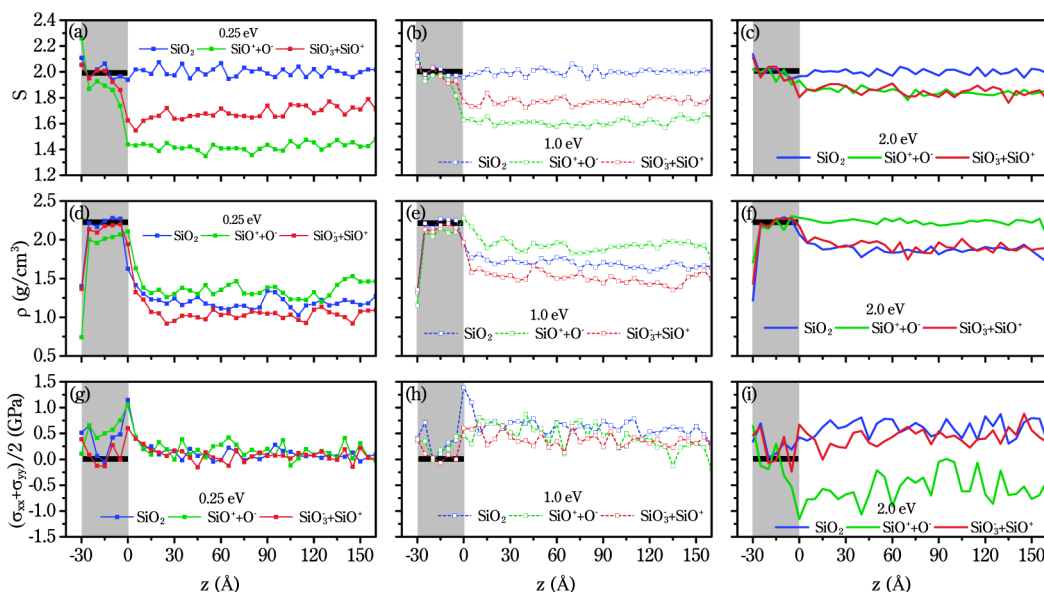


**Figure 2.** Local  $(x,y)$ -averaged properties of the films as a function of  $z$ : (a–c) stoichiometry, i.e., the number of oxygen per silicon; (d–f) mass density; (g–i) in-plane stress  $[(\sigma_{xx} + \sigma_{yy})/2]$ . The shaded gray area depicts the substrate position. Black lines show bulk values of the corresponding properties.

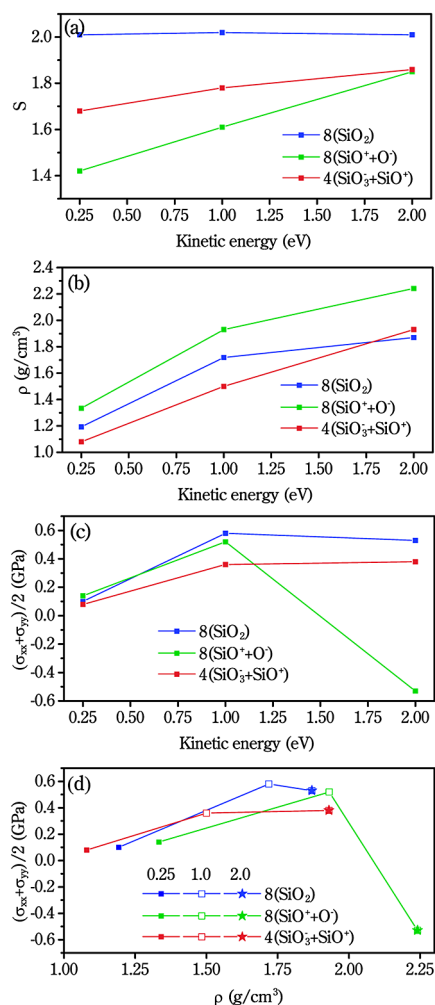


**Figure 3.** Local film properties vs  $E$  for the three incoming fluxes considered: (a) stoichiometry; (b) mass density; (c) in-plane stress; (d) in-plane stress vs density.

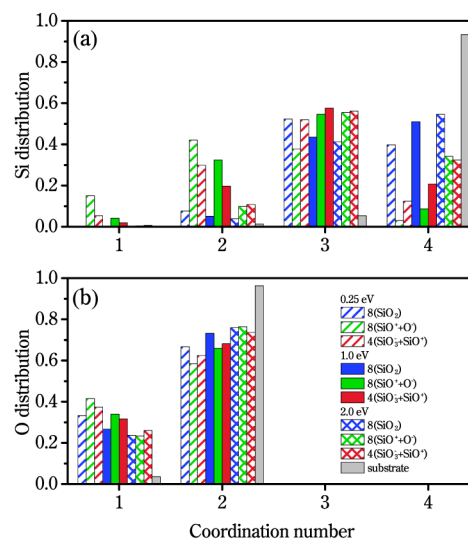


**Figure 4.** Coordination number of different deposition schemes vs  $E$ .

information. The notion of porosity only emerges at the mesoscopic scale via the consideration of a probe of finite size. For the sake of simplicity, we only consider spherical probes, the radius  $R$  of which is hence the key parameter of the analysis.

As detailed in the dedicated section of the [Supporting Information](#), the analysis proceeds first by the identification of all of the (probe-accessible) points, where such a probe fits in without approaching any atom below the atomic radius. The porosity then consists of all the (probe-occupiable) points that can be covered by such a probe. In our film, the porosity further splits into two types of structures:

- a main channel, which consists of all pores that connect to the open surface, i.e., through which a probe of radius  $R$  coming from the outside of the films can diffuse.
- isolated pockets that are disconnected from the main channel.

We did not observe any indication of the existence of channels that would percolate transversely to the film without connecting

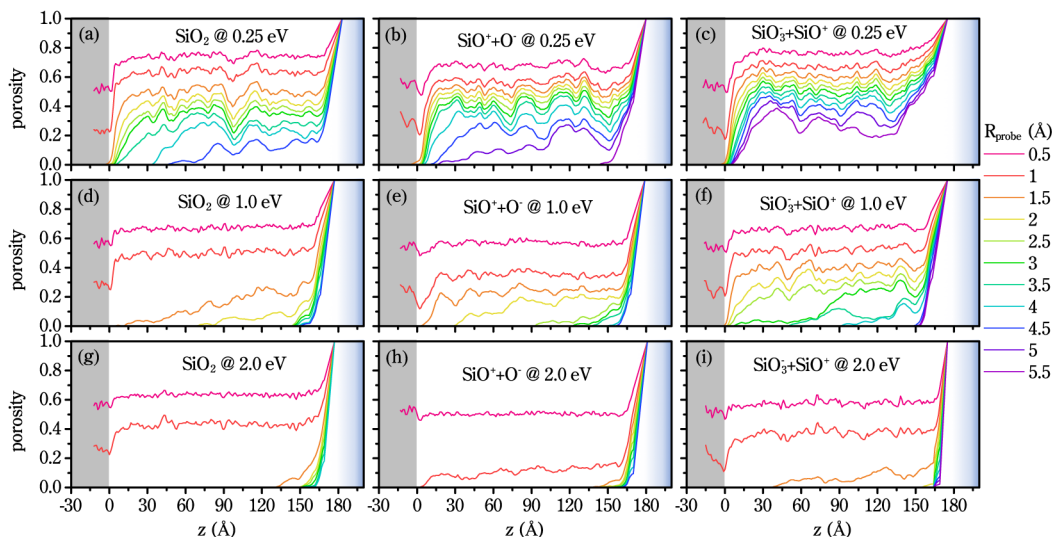


**Figure 5.** Porosity of the main channel ( $\varphi_{\text{main}}$ ) as a function of  $z$ . The upper row (a–c) is for  $E = 0.25$  eV; the middle row (d–f) is for  $E = 1.0$  eV; the lower row (g–i) is for  $E = 2.0$  eV. Columns from left to right correspond to different deposition species:  $8(\text{SiO}_2)$ ,  $8(\text{SiO}^+ + \text{O}^-)$  and  $4(\text{SiO}_3^- + \text{SiO}^+)$ . The gray area depicts the substrate position.

to the main channel. This leads us to characterize the porosity of our films via the volume fractions  $\varphi_{\text{main}}$  and  $\varphi_{\text{pockets}}$  occupied by, respectively, the main channel and isolated pockets. In the [Supporting Information](#), we demonstrate that both  $\varphi_{\text{total}} = \varphi_{\text{main}} + \varphi_{\text{pockets}}$  and  $\varphi_{\text{main}}$  are decreasing functions of  $R$ .

The main results of our analysis are now displayed in two figures. [Figure 5](#) presents, for each film and for a few probe radii regularly spaced between 0.5 and 5.5 Å, the fraction of space occupied by the main channel,  $\varphi_{\text{main}}(z)$  vs  $z$ , as averaged over  $x$  and  $y$ . [Figure 6](#) examines, as a function of  $R$ , both  $\bar{\varphi}_{\text{main}}$  and  $\bar{\varphi}_{\text{pockets}}$ , as averaged over the whole films [i.e., on  $(x, y, z)$ ].

As we expected,  $\varphi_{\text{main}}$  appears to be a decreasing function of  $R$  in both [Figures 5](#) and [6](#). The volume fraction of isolated pockets, however, is not necessarily monotonically decreasing with  $R$ : the increasing  $R$  may cause parts of percolation channels to become inaccessible, i.e., to transform into isolated pockets.

The films produced at the lowest impact kinetic energy,  $E = 0.25$  eV (top row of [Figure 5](#) and panel (a) of [Figure 6](#)), demonstrate a very high degree of porosity. In all three deposition cases, for probe radii of up to about 3 Å, the main channel occupies more than 50% of the films and extends almost down to the substrate.

Let us continue to examine the  $E = 0.25$  eV films while focusing on probe radii  $R \lesssim 3.5$  Å. [Figure 6a](#) demonstrates that  $\bar{\varphi}_{\text{main}} \gg \bar{\varphi}_{\text{pockets}}$  over this whole  $R$ -range, so that  $\bar{\varphi}_{\text{total}} \simeq \bar{\varphi}_{\text{main}}$ : there is essentially a single macropore as the whole porosity of the films participates in the main channel only. It follows that the decrease of  $\bar{\varphi}_{\text{main}}$  with  $R$  over this range results almost entirely from the narrowing of the probe-accessible volume, and not from a change in pore connectivity. Finally, over the same  $R$ -range, the local porosity  $\varphi_{\text{main}}(z)$  displayed in the top row of [Figure 5](#) [see panels (a–c)] is nearly  $z$ -independent (up to finite-size fluctuations) in the bulk of the films, i.e., away from the surface and substrate. Since the pockets are then essentially absent, i.e.,  $\varphi_{\text{total}}(z) \simeq \varphi_{\text{main}}(z)$ , this observation demonstrates that the pore space is quite homogeneous throughout the film.

As  $R$  increases beyond 3.5 or 4 Å,  $\bar{\varphi}_{\text{pockets}}$  measurably increases and eventually exceeds  $\bar{\varphi}_{\text{main}}$  [see [Figure 6a](#)], showing that a measurable fraction of the porosity transitions to local pockets.

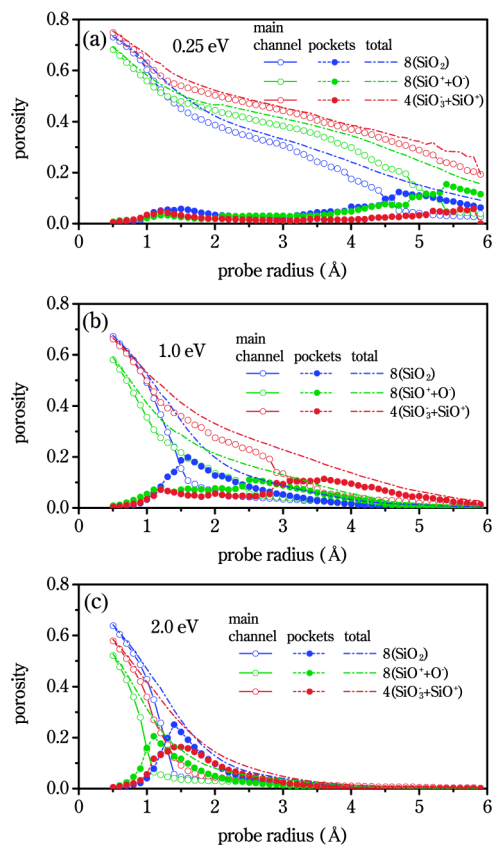


**Figure 6.** Average porosity characterized by the total volume fraction of pores ( $\bar{\varphi}_{\text{total}} = \bar{\varphi}_{\text{main}} + \bar{\varphi}_{\text{pockets}}$ , dashed-dotted), that of the main channel ( $\bar{\varphi}_{\text{main}}$ , hollow circles), and that of isolated pockets ( $\bar{\varphi}_{\text{pockets}}$ , filled circles) pores, as a function of probe radius  $R$ , for different deposition cases: (a)  $E = 0.5$  eV, (b)  $E = 1.0$  eV, and (c)  $E = 2.0$  eV.

This hence marks very clearly a change of connectivity, i.e., a splitting of the main (macro) pore into pockets. In the local data of [Figure 5a–c](#), this transition is accompanied by a loss of homogeneity of the main channel fraction  $\varphi_{\text{main}}(z)$ , which first starts to decrease toward the substrate, then vanishes at the

lowest  $z$ . With the increasing probe size  $R$ , as probe-accessible passage points close down, the percolation to low  $z$  values becomes increasingly unlikely, and the main channel is progressively more localized near the upper part of the film.

Let us now examine the films produced with a higher impact kinetic energy in the middle and bottom rows of Figure 5 and in panels (b) and (c) of Figure 6. The features observed at  $E = 0.25$  eV can be recovered, but in a much narrower  $R$  range. At small  $R$ , indeed, the films systematically present a homogeneous macropore with  $\bar{\varphi}_{\text{total}} \simeq \bar{\varphi}_{\text{main}} \gg \bar{\varphi}_{\text{pockets}}$ ; the total pore fraction initially decreases with  $R$  without a significant increase of  $\bar{\varphi}_{\text{pockets}}$ , i.e., without any change of connectivity. At higher  $R$  values (which depend on growth conditions), the pocket fraction,  $\bar{\varphi}_{\text{pockets}}$ , eventually rises, which then marks a change of connectivity: this systematically corresponds to the vanishing of  $\bar{\varphi}_{\text{main}}(z)$  near the substrate, i.e., to a significant connectivity change and the progressive localization of the main channel near the upper part of the film.

The extent of the main channel can be characterized by the coordinate of its lowest point,  $z_{\text{min}}$ , which is displayed in Figure 7

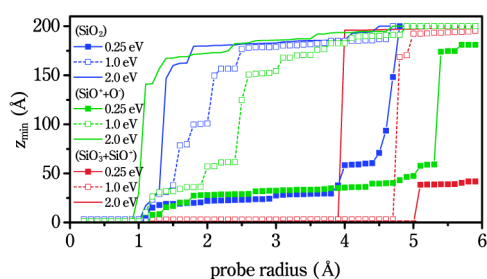


**Figure 7.** Penetration of the main channel characterized by the coordinate  $z_{\text{min}}$  of its lowest point.

as a function of the probe size for the nine deposition conditions explored. Although this measure may be sensitive to sample-to-sample fluctuations, the trends it displays are very consistent with the overall picture emerging from our analysis. The value of  $z_{\text{min}}$  necessarily increases with  $R$ , since  $\bar{\varphi}_{\text{main}}(z)$  decreases with  $R$  at any  $z$ , as we have shown. It appears that  $z_{\text{min}}$  approaches the top of the substrate for the smallest radii and remains in its vicinity up to large values of  $R$  for the films produced at  $E = 0.25$  eV, and for all the films examined in case (III). These data, hence, clearly document the possibility of obtaining highly porous films comprising channels that extend almost all the way down to the substrate, even for rather large probes of several Ångströms in radius.

In most cases, the narrowing of the main channel (the rise of  $z_{\text{min}}$ ) takes place rather abruptly, within an Ångström of change in  $R$ . This can be seen in all of our films except for that produced in case (III) with  $E = 0.25$  eV, for which this transition is not visible in the studied  $R$  range. The value of  $R$  at which this narrowing takes place provides a rough characterization of the size of the channel pores. It clearly decreases with the increasing  $E$ , i.e., with the increasing film density, as expected, and reaches barely a couple of Ångströms for the films produced at  $E = 1.0$  and  $2.0$  eV in cases (I) and (II), which demonstrates a very limited porosity.

An intriguing feature of the above observations is that it was possible to obtain a very porous film in case (III) even at the highest value of the kinetic energy,  $E = 2.0$  eV. This film has nearly the same density [see Figure 3b] as the case (II) film with

the same value of  $E$ , for which the main channel is localized at the very surface of the film as soon as  $R$  exceeds an Ångström.

**Impact Events and Growth Mechanisms.** In order to shed light on the mechanisms giving rise to the growth of porous structures, we examined impact events in detail.

To start, let us gather, in Figure 8, information about the deposition (sticking) probabilities of both the impinging ions

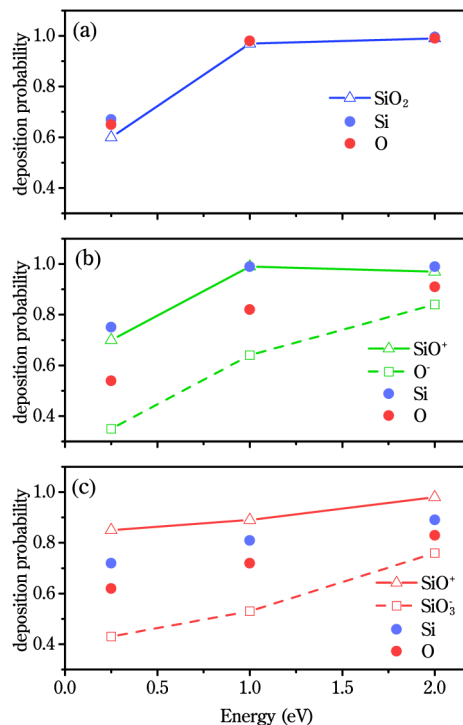


**Figure 8.** Deposition probability of molecules/ions as a function of energy for different deposition cases: (a)  $8(\text{SiO}_2)$ ; (b)  $8(\text{SiO}^+ + \text{O}^-)$ ; (c)  $4(\text{SiO}_3^- + \text{SiO}^+)$ .

and individual atoms. As anticipated, these probabilities visibly depart from unity, meaning that a measurable fraction of the incident atoms rebound.

The loss of matter may involve three mechanisms: (i) impinging ions or molecules may rebound on the film as whole units; (ii) they may dissociate during impact and leave some of their atoms in the film, while others rebound; (iii) impacts may sputter atoms already present in the film. By examining the list of atoms eliminated from the simulation at step 3 in the algorithm, we could precisely evaluate the relative importance of these effects and found that the last two cases occur very rarely under the studied low- $E$  conditions: case (ii) is relevant for  $\sim 1$  to 2% of ions, and case (iii) accounts for less than 0.1% of nondeposited atoms. Thus, our analysis will be guided by the idea that, in all our films, ions or molecules stick to the growing film or rebound, essentially as whole units.

In case (I) [deposition of  $\text{SiO}_2$ , in Figure 8a], the sticking probabilities are very close to 1 for incident particle energies above 1.0 eV, and drop almost 2-fold, to  $\sim 60\%$ , at an energy of 0.25 eV. The slight discrepancy between the sticking probabilities of  $\text{SiO}_2$  vs silicon and oxygen atoms at  $E = 0.25$  eV results from the small number of events involving the breakup of the impinging molecule.

In the two other cases [ $(\text{SiO}^+ + \text{O}^-)$  and  $(\text{SiO}_3^- + \text{SiO}^+)$ , in panels (b) and (c), respectively, in Figure 8], the sticking

probabilities also tend to grow with  $E$ , and they are systematically higher for positively charged ions than for negatively charged ones. This effect is measurable over the entire incident energy range but tends to be stronger at lower  $E$  values. A small discrepancy between the sticking probabilities of  $\text{SiO}^+$  and atomic silicon can be seen in case (II) at  $E = 0.25$  eV; it results from the rare  $\text{SiO}^+$  dissociation events. It is also noteworthy that  $\text{SiO}^+$  is involved in both cases (II) and (III) but it displays visibly different deposition probabilities in either case. This observation demonstrates that the statistical outcomes of deposition events sensitively depend on the structure of the growing film (e.g., its porosity and stoichiometry), which itself depends on the growth conditions. It hence points to the existence of a feedback mechanism between the development of heterogeneities and impact processes, the latter being likely to be strongly influenced by the long-range (Coulombic) interaction between the growing surface and impinging particles.

Since molecular ion dissociation upon impact is rare, the sticking probabilities of ions and atomic species are tightly interrelated. For instance, in case (II) [deposition of  $\text{SiO}^+ + \text{O}^-$ ], the sticking probability of Si is  $s_{\text{Si}} \simeq s_{\text{SiO}^+}$ , while that of O is  $s_{\text{O}} \simeq (s_{\text{SiO}^+} + s_{\text{O}^-})/2$ , where  $s_{\text{SiO}^+}$  and  $s_{\text{O}^-}$  are the sticking probabilities of the two considered ions. It follows that the final stoichiometry of the films is determined by the differential sticking probabilities of the incoming ions and explains our measurements of  $S$ , as shown in Figure 2: the  $\text{SiO}_2$  influx of case (I) leads to the formation of nearly stoichiometric silica due to the quasi-absence of dissociation; meanwhile, the differential sticking probabilities between positively and negatively charged ions entail that the influxes of either  $\text{SiO}^+$  and  $\text{O}^-$  or  $\text{SiO}_3^-$  and  $\text{SiO}^+$  produce more oxygen-deficient films, especially at the lower impacting velocities.

Rebounds occur because, on their way toward the surface, impinging particles may encounter high energy barriers that may prevent them from reaching distances at which they form chemical bonds. These barriers, since they lie beyond the chemical bonding range, are necessarily of Coulombic origin and result from the existence of charge heterogeneities on the growing surface.

In order to illustrate this issue, we have calculated the total Coulombic potential  $U(x,y,z)$  induced by the atoms of the film on a  $q_p = +e$  probe at arbitrary locations, while using the same upper cutoff (10 Å) as the ReaxFF potential. We show in the Supporting Information the 2D maps of  $U(x,y,z)$  at a fixed height  $h = z - z^{\text{top}} = 1.5$  Å above the topmost atom in the film to illustrate the strong heterogeneity of this potential, which arises from both the porosity and the polarization between oxygen and silicon atoms.

Vertical cuts of  $U(x,y,z)$  are presented in the left column of Figure 9, while focusing on  $z \in [z^{\text{top}} - 45 \text{ Å}, z^{\text{top}} + 5 \text{ Å}]$  to image the upper atomic layers, which interact with an impinging particle. Figure 9 also presents the local charge (center column) and mass (right column) densities at the same locations. A close examination and comparison of these fields show that the Coulombic potential  $U(x,y,z)$  tends to be predominantly negative (blue shades) inside pores and in the topmost layers of the films. The films, however, are globally neutral due to charge equilibration, which is properly taken into account in the LAMMPS implementation of the ReaxFF potential. The observed predominance of negative  $U(x,y,z)$  values in pores and directly above the upper layers of the film hence manifests the existence of a polarization of the silica surface, the latter

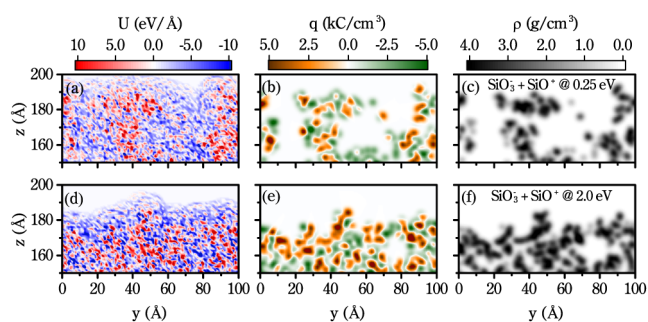


**Figure 9.** For the two films produced in case (III) at  $E = 0.25$  eV (top) and  $E = 2.0$  eV (bottom), cuts of various fields in the  $(y,z)$  plane at  $x = 50$  Å: Coulombic contribution to the potential energy  $U(x,y,z)$  (left), charge density (middle), and mass density (right). Both mass and charge densities have been smoothed by Gaussian broadening of the width of 2 Å.

being defined as the boundary between dense matter and open spaces. Since oxygen and silicon tend to present opposite charges (negative and positive, respectively), this polarization reflects a systematic bias in how silicon and oxygen atoms are organized near the surface, which we interpret as follows: due to its ability to form up to four chemical bonds, silicon tends to surround itself with oxygen atoms and thus to embed itself slightly deeper than the latter; the silicon positive charges hence tend to be slightly masked by the oxygen negative ones, which leads to the observed polarization of the surface.

Due to this polarization, the impinging particles experience a systematically biased interaction with the growing surface depending on their charge. This explains that negatively charged particles tend to rebound with a higher probability than positively charged ones, thus leading to an overall non-stoichiometry of the growing films.

It is noteworthy that low  $E$  values give rise both to highly porous films and higher rebounding probabilities, and we hence must ask whether these two properties are interrelated. The connection, we think, is that since the surface of the growing film is highly heterogeneous, low- $E$  particles should be significantly deflected along the  $(x,y)$  plane. In some cases, this deflection of the trajectory leads to a rebound; in others, the particles are incorporated yet after sustaining a significant drift. We have quantified this phenomenon by systematically analyzing in the Supporting Information the statistics of atomic transverse deflections [along the  $(x,y)$  plane] during impacts.

The key outcome of this analysis is that the impinging particles tend to be increasingly deflected with decreasing  $E$ , and all the more so that they are light and charged. This, we think, is a driving factor in the mechanism of pore growth, since the latter evidently requires significant lateral motion of the incoming particle. Indeed, if the particles were not deflected at all or barely, the films would tend to grow homogeneously, with little roughness. In order to illustrate this point, we present three movies in the Supporting Information, which show, in cases (I), (II), and (III), the trajectories of Si atoms during a few impact events at  $E = 0.25$  eV. Here, the films have already developed a significant degree of porosity. It is visible from the movie obtained in case (I) that  $\text{SiO}_2$  particles are barely deflected, as our above analysis has shown. In case (II), we only image  $\text{SiO}^+$  ions, and it is very clear that they are systematically and significantly deflected toward the sides (surfaces) of growing pores. This sideward motion prevents the incoming ions from filling the hole below their point of arrival and thus directly

contributes to pore formation. The same can be seen in case (III) for both involved ions.

Thus, we conclude that pores are formed at low  $E$  due to the preimpact deflection of incoming particles by surface charge heterogeneities. Besides, since low kinetic energy also leads to a higher rebound probability (since the Coulombic barriers are more unlikely to be overcome), and to a higher contrast between the rebound probabilities of positively and negatively charged ions, we finally expect that low- $E$  films tend to grow both porous and nonstoichiometric.

## CONCLUSION

To summarize, we have implemented for the first time an MD simulation of low- $T$  deposition based on the ReaxFF, which enables us to correctly take into account the reactive incorporation of impinging particles, as well as charge and polarization effects. A minimization technique was used to efficiently remove the excess energy brought by impacts and thus account for the fact that, under usual experimental conditions, heat flows are efficient enough that films grow near room temperature (at most about 100 °C), which is much below typical glass transition temperatures for oxides. This algorithm was implemented to study growth conditions in which the kinetic energy  $E$  of impinging particles is relatively low, i.e., corresponds to at most a very few eV. Since the introduction of an inert gas in a deposition chamber reduces  $E$  via collisional slowing down and since we expect sputtering to produce faster particles, this range of values is experimentally accessible, in principle.

Previous studies<sup>8,9</sup> have pointed out that atomic oxygen has a higher rate of rebound than other species, so a stoichiometric influx of atomic silicon and oxygen cannot produce stoichiometric films. However, stoichiometric silica films can be deposited by sputtering a silica target without an oxygen gas feed.<sup>12–14</sup> It follows that such sputtering conditions should involve a stoichiometric flux of particles in which silicon and oxygen are already covalently bonded.<sup>3</sup> Due to the lack of information about the nature of the sputtered ions in typical experimental setups (such as e-beam or ion-beam sputtering), we have explored a few options for the composition of the impinging plume as an unknown parameter: (I) SiO<sub>2</sub>; (II) SiO<sup>+</sup> and O<sup>-</sup>; (III) SiO<sub>3</sub><sup>-</sup> and SiO<sup>+</sup>. The comparison of these conditions enabled us to shed light on the effects associated with the type of impinging ions.

Our study of insertion events showed that ions only very rarely dissociate upon impact at the studied (low)  $E$  values: in less than ~1–2% of cases, some of their atoms rebound while others stick to the film. In the vast majority of cases, impinging ions either rebound or incorporate into the film as whole units. We expect this observation to apply quite broadly for moderate kinetic energies, i.e., for  $E$  values that are significantly smaller than the energy of formation of covalent bonds. It follows that the final stoichiometry of the films is determined essentially by the differential rebounding rate between ion species. This finding generalizes previous studies about differential sticking probabilities between single atoms.<sup>8,9</sup>

We have shown that low- $E$  growth favors the formation of tensile and porous films and obtained a thorough characterization of the porosity. We pointed out that the formation of pores necessarily involves significant transverse displacements of impinging particles and observed that this was favored by the charge heterogeneity of the surface of the film, which is an intrinsic feature of silica, resulting from the fact that silicon and

oxygen tend to carry charges of opposite signs. More precisely, the surfaces of the growing pores, like the top layers of the film, are polarized because silicon atoms (which carry positive charges) surround themselves with oxygen atoms (which carry negative charges) and tend to lie slightly inward, thus cloaking themselves and the charge they carry.

The polarization of the growing silica surface causes the rebound probability to be higher for negatively charged ions. It also tends to favor the formation of pores. When a film grows, indeed, it may develop a certain roughness due to the stochastic nature of the process, leading to the possible formation of protrusions and troughs that are the precursors of the pores. Troughs or emerging pores are, by definition, encased between material surfaces, i.e., regions where the long-range Coulombic effects of multiple surfaces add up: this is why the Coulombic energy  $U(x,y,z)$  appeared predominantly negative throughout the pores in Figure 9. This enhancement of Coulombic contributions tends to deflect more strongly negatively charged impinging particles away from the pores. The movies we provide clearly show that, in the late stage of their arrival upon the film, slow impinging particles are deflected toward the protrusions, thus preventing them from filling in a trough. This mechanism is presumably the main driver of pore formation.

The polarization-induced deflection of impinging particles near the surface is, of course, all the more significant when particles are slow, which explains why low  $E$  values correlate both with larger values of the preimpact transverse shift of the impinging ions and with a higher degree of porosity. These effects may also be sensitive to the shape and size of particles: we have some indication that this could be the case since our case (III) films present a significantly larger porosity than case (II), but we did not explore the issue further.

This interpretation of the mechanism giving rise to pore growth is also consistent with our observation that the kinetic energy of impinging particles seems to be the main determinant of the film density and porosity. Indeed, although we have emphasized the differences between the films produced in cases (I), (II), and (III), we could as well point out similarities: the case-to-case differences in density, for example, are significantly smaller than the overall range of values (from around 1.2 g/cm<sup>3</sup> at  $E = 0.25$  eV to around 2.0 g/cm<sup>3</sup> at  $E = 2.0$  eV); likewise, the fractions occupied by the main channel or by pockets, for various probe sizes [see Figure 6], present more similarities between the three studied cases, than when varying  $E$  over the studied range.

Finally, our analysis of the film porosity demonstrated that for our lowest  $E$  value, the main percolation channel connected to the space above the film could extend down to the substrate, even for quite large probe sizes (radii of 4 or even 5 Å).

Although we have obtained these observations through the analysis of a specific numerical model, necessarily based on precise (hence disputable) assumptions concerning the impinging particles or the force field, we believe that the identified phenomena leading to pore formation at low impact kinetic energy are general enough to be operative across a broad range of impinging particle compositions. Although such deposition conditions are not usually studied since most experimental efforts usually target the densest and most homogeneous films, they could be achieved experimentally via kinetic slowing down by introducing a neutral gas in the chamber.

## ■ ASSOCIATED CONTENT

### SI Supporting Information

The Supporting Information is available free of charge at <https://pubs.acs.org/doi/10.1021/acs.jpcc.4c02198>.

Additional details on microstructural characteristics (Figure S1); porosity analysis (Figures S2 and S3); surface charges and Coulombic effects (Figures S4 and S5); ion deflections during impacts (Figures S6 and S7) (PDF)

Movies of impacts on the growing film in cases (I), (II), and (III) for  $E = 0.25$  eV (ZIP)

## ■ AUTHOR INFORMATION

### Corresponding Author

Anaël Lemaître – Navier, Ecole des Ponts, Univ Gustave Eiffel, CNRS, Marne-la-Vallée 77420, France; [orcid.org/0000-0002-6865-9245](https://orcid.org/0000-0002-6865-9245); Email: [anael.lemaître@enpc.fr](mailto:anael.lemaître@enpc.fr)

### Authors

Nikita S. Shcheblanov – MSME, Univ Gustave Eiffel, CNRS, Univ Paris Est Créteil, UMR 8208, Marne-la-Vallée 77454, France; [orcid.org/0000-0001-8696-2435](https://orcid.org/0000-0001-8696-2435)

Céline Léonard – MSME, Univ Gustave Eiffel, CNRS, Univ Paris Est Créteil, UMR 8208, Marne-la-Vallée 77454, France; [orcid.org/0000-0003-0303-3505](https://orcid.org/0000-0003-0303-3505)

Quy-Dong To – MSME, Univ Gustave Eiffel, CNRS, Univ Paris Est Créteil, UMR 8208, Marne-la-Vallée 77454, France; [orcid.org/0000-0001-9257-835X](https://orcid.org/0000-0001-9257-835X)

Mikhail E. Povarnitsyn – Navier, Ecole des Ponts, Univ Gustave Eiffel, CNRS, Marne-la-Vallée 77420, France; [orcid.org/0000-0003-1990-1688](https://orcid.org/0000-0003-1990-1688)

Complete contact information is available at: <https://pubs.acs.org/doi/10.1021/acs.jpcc.4c02198>

### Notes

The authors declare no competing financial interest.

## ■ ACKNOWLEDGMENTS

This work has benefited from a French government grant managed by ANR within the frame of the national program Investments for the Future ANR-11-LABX022-01 (LabEx MMCD project).

## ■ ADDITIONAL NOTE

<sup>a</sup>The atoms lying near the upper and lower boundaries are included in this analysis, but do not introduce a measurable error since they constitute very small fractions of the atoms in the films.

## ■ REFERENCES

- (1) Mattox, D. M. *Handbook of physical vapor deposition (PVD) processing*; William Andrew, Elsevier Science: Oxford: Norwich, N.Y., 2010.
- (2) Mahan, J. E. *Physical vapor deposition of thin films*; Wiley: New York, 2000.
- (3) Gelin, S.; Poinot, D.; Chatel, S.; Calba, P.-J.; Lemaître, A. Microstructural origin of compressive in situ stresses in electron-gun-evaporated silica thin films. *Phys. Rev. Mater.* **2019**, *3*, 055608.
- (4) Sigmund, P. *Sputtering by Particle Bombardment I: Physical Sputtering of Single-Element Solids*; Behrisch, R., Ed.; Springer: Berlin, Heidelberg, 1981; pp. 971.
- (5) Yamamura, Y. Theory of sputtering and comparison to experimental data. *Nucl. Instrum. Methods Phys. Res.* **1982**, *194*, 515–522.
- (6) Sigmund, P. Mechanisms and theory of physical sputtering by particle impact. *Nucl. Instrum. Methods Phys. Res., Sect. B* **1987**, *27*, 1–20.
- (7) Berg, S.; Nyberg, T. Fundamental understanding and modeling of reactive sputtering processes. *Thin Solid Films* **2005**, *476*, 215–230.
- (8) Lefèvre, A.; Lewis, L. J.; Martinu, L.; Wertheimer, M. R. Structural properties of silicon dioxide thin films densified by medium-energy particles. *Phys. Rev. B* **2001**, *64*, 115429.
- (9) Taguchi, M.; Hamaguchi, S. Molecular dynamics study on Ar ion bombardment effects in amorphous SiO<sub>2</sub> deposition processes. *J. Appl. Phys.* **2006**, *100*, 123305.
- (10) Taguchi, M.; Hamaguchi, S. MD simulations of amorphous SiO<sub>2</sub> thin film formation in reactive sputtering deposition processes. *Thin Solid Films* **2007**, *515*, 4879–4882.
- (11) Robic, J. Y.; Leplan, H.; Pauleau, Y.; Rafin, B. Residual stress in silicon dioxide thin films produced by ion-assisted deposition. *Thin Solid Films* **1996**, *290–291*, 34–39.
- (12) Tabata, A.; Matsuno, N.; Suzuoki, Y.; Mizutani, T. Optical properties and structure of SiO<sub>2</sub> films prepared by ion-beam sputtering. *Thin Solid Films* **1996**, *289*, 84–89.
- (13) Ji, Y. Q.; Jiang, Y.; Liu, H. S.; Wang, L.; Liu, D. D.; Jiang, C. H.; Fan, R. W.; Chen, D. Y. Optical Constants of SiO<sub>2</sub> Films Deposited on Si Substrates. *Chin. Phys. Lett.* **2014**, *31*, 046401.
- (14) Mateev, M.; Lautenschläger, T.; Spemann, D.; Finzel, A.; Gerlach, J. W.; Frost, F.; Bundesmann, C. Systematic investigation of the reactive ion beam sputter deposition process of SiO<sub>2</sub>. *Eur. Phys. J. B* **2018**, *91*, 45.
- (15) Grigoriev, F. V.; Sulimov, A. V.; Kochikov, I.; Kondakova, O. A.; Sulimov, V. B.; Tikhonravov, A. V. High-performance atomistic modeling of optical thin films deposited by energetic processes. *Int. J. High Perform. Comput. Appl.* **2015**, *29*, 184–192.
- (16) Gorokh, A. A.; Grigoriev, F. V.; Katkova, E. V.; Sulimov, A. V.; Sharapova, S. A. High-performance modeling of the deposition of a silicon dioxide thin film using the LAMMPS program. *Moscow Univ. Phys. Bull.* **2016**, *71*, 114–117.
- (17) Grigoriev, F. V.; Katkova, E. V.; Sulimov, A. V.; Sulimov, V. B.; Tikhonravov, A. V. Annealing of deposited SiO<sub>2</sub> thin films: Full-atomistic simulation results. *Opt. Mater. Express* **2016**, *6*, 3960–3966.
- (18) Grigoriev, F. V.; Sulimov, A. V.; Katkova, E. V.; Kochikov, I. V.; Kondakova, O. A.; Sulimov, V. B.; Tikhonravov, A. V. Full-atomistic nanoscale modeling of the ion beam sputtering deposition of SiO<sub>2</sub> thin films. *J. Non-Cryst. Solids* **2016**, *448*, 1–5.
- (19) Grigoriev, F. V.; Sulimov, V. B.; Tikhonravov, A. V. Thin films structural properties: Results of the full-atomistic supercomputer simulation. *Proceedings of the SPIE 10603, Photonics, Devices, and Systems VII*; SPIE, 2017.
- (20) Grigoriev, F.; Sulimov, A.; Kochikov, I.; Kondakova, O.; Sulimov, V.; Tikhonravov, A. Computational experiments on atomistic modeling of thin-film deposition. *Appl. Opt.* **2017**, *56*, C87–C90.
- (21) Zhupanov, V. G.; Grigoriev, F. V.; Sulimov, V. B.; Tikhonravov, A. V. The Validity of the Results of High-Performance Modeling of SiO<sub>2</sub> Film Growth. *Moscow Univ. Phys. Bull.* **2017**, *72*, 558–562.
- (22) Grigoriev, F.; Sulimov, V.; Tikhonravov, A. Simulation of the optical coating deposition. *Adv. Opt. Technol.* **2018**, *7*, 13–22.
- (23) Grigoriev, F. V.; Sulimov, V. B.; Tikhonravov, A. V. Atomistic simulation of the glancing angle deposition of SiO<sub>2</sub> thin films. *J. Non-Cryst. Solids* **2019**, *512*, 98–102.
- (24) Grigoriev, F. V.; Sulimov, V. B.; Tikhonravov, A. Combined Modeling of the Optical Anisotropy of Porous Thin Films. *Coatings* **2020**, *10*, 517.
- (25) Grigoriev, F. V.; Sulimov, V. B.; Tikhonravov, A. V. Atomistic Simulation of Stresses in Growing Silicon Dioxide Films. *Coatings* **2020**, *10*, 220.
- (26) Grigor'ev, F. V.; Sulimov, V. B.; Tikhonravov, A. V. Molecular Dynamics Modeling of the Deposition of Thin Films Consisting of

Layers of Alternating Density. *Russ. J. Phys. Chem. A* **2020**, *94*, 979–983.

(27) Grigoriev, F. V.; Sulimov, V. B.; Tikhonravov, A. V. Application of a large-scale molecular dynamics approach to modelling the deposition of TiO<sub>2</sub> thin films. *Comput. Mater. Sci.* **2021**, *188*, 110202.

(28) Grigoriev, F. V.; Sulimov, V. B.; Tikhonravov, A. V. Atomistic Simulation of the Ion-Assisted Deposition of Silicon Dioxide Thin Films. *Nanomaterials* **2022**, *12*, 3242.

(29) Grigoriev, F. V.; Sulimov, V. B. Atomistic Simulation of Physical Vapor Deposition of Optical Thin Films. *Nanomaterials* **2023**, *13*, 1717.

(30) Grigoriev, F. V.; Sulimov, V. B.; Tikhonravov, A. V. Silicon Dioxide Thin Films Deposited Using Oxide Targets: Results of Atomistic Simulation. *Coatings* **2024**, *14*, 258.

(31) Baumann, S. M.; Martner, C. C.; Martin, D. W.; Blattner, R. J.; Braundmeier, A. J. A study of electron beam evaporated SiO<sub>2</sub>, TiO<sub>2</sub>, and Al<sub>2</sub>O<sub>3</sub> films using RBS, HFS, and SIMS. *Nucl. Instrum. Methods Phys. Res., Sect. B* **1990**, *45*, 664–668.

(32) Klevenz, M.; Wetzels, S.; Möller, M.; Pucci, A. Evaporation and Condensation of SiO and SiO<sub>2</sub> Studied by Infrared Spectroscopy. *Appl. Spectrosc.* **2010**, *64*, 298–303.

(33) Devanathan, R. *Handbook of Materials Modeling: Applications: Current and Emerging Materials*; Andreoni, W.; Yip, S., Ed.; Springer International Publishing: Cham, 2020; pp. 21412159.

(34) van Duin, A. C. T.; Dasgupta, S.; Loran, F.; Goddard, W. A. ReaxFF: A Reactive Force Field for Hydrocarbons. *J. Phys. Chem. A* **2001**, *105*, 9396–9409.

(35) Senftle, T. P.; Hong, S.; Islam, M. M.; Kylasa, S. B.; Zheng, Y.; Shin, Y. K.; Junkermeier, C.; Engel-Herbert, R.; Janik, M. J.; Aktulga, H. M. The ReaxFF reactive force-field: Development, applications and future directions. *Npj Comput. Mater.* **2016**, *2*, 15011.

(36) Rimsza, J. M.; Yeon, J.; van Duin, A. C. T.; Du, J. Water Interactions with Nanoporous Silica: Comparison of ReaxFF and ab Initio based Molecular Dynamics Simulations. *J. Phys. Chem. C* **2016**, *120*, 24803–24816.

(37) Hahn, S. H.; Rimsza, J.; Criscenti, L.; Sun, W.; Deng, L.; Du, J.; Liang, T.; Sinnott, S. B.; van Duin, A. C. T. Development of a ReaxFF Reactive Force Field for NaSiO<sub>x</sub>/Water Systems and Its Application to Sodium and Proton Self-Diffusion. *J. Phys. Chem. C* **2018**, *122*, 19613–19624.

(38) Nayir, N.; van Duin, A. C. T.; Erkoç, S. Development of the ReaxFF Reactive Force Field for Inherent Point Defects in the Si/Silica System. *J. Phys. Chem. A* **2019**, *123*, 4303–4313.

(39) Nayir, N.; van Duin, A. C. T.; Erkoç, S. Development of a ReaxFF Reactive Force Field for Interstitial Oxygen in Germanium and Its Application to GeO<sub>2</sub>/Ge Interfaces. *J. Phys. Chem. C* **2019**, *123*, 1208–1218.

(40) Hahn, S. H.; van Duin, A. C. T. Surface Reactivity and Leaching of a Sodium Silicate Glass under an Aqueous Environment: A ReaxFF Molecular Dynamics Study. *J. Phys. Chem. C* **2019**, *123*, 15606–15617.

(41) Wang, Y.; Shi, Y.; Sun, Q.; Lu, K.; Kubo, M.; Xu, J. Development of a Transferable ReaxFF Parameter Set for Carbon- and Silicon-Based Solid Systems. *J. Phys. Chem. C* **2020**, *124*, 10007–10015.

(42) Krishnan, N. M. A.; Wang, B.; Yu, Y.; Le Pape, Y.; Sant, G.; Bauchy, M. Enthalpy Landscape Dictates the Irradiation-Induced Disorder of Quartz. *Phys. Rev. X* **2017**, *7*, 031019.

(43) Chuon, S. *Simulation numérique multi-échelles du procédé de dépôt par pulvérisation cathodique magnétron*, Doctoral dissertation, Université d'Orléans; Universiteit Antwerpen, 2019.

(44) Hirvonen, J. K. Ion beam assisted thin film deposition. *Mater. Sci. Rep.* **1991**, *6*, 215–274.

(45) Bundesmann, C.; Neumann, H. Tutorial: The systematics of ion beam sputtering for deposition of thin films with tailored properties. *J. Appl. Phys.* **2018**, *124*, 231102.

(46) Hawkeye, M. M.; Brett, M. J. Glancing angle deposition: Fabrication, properties, and applications of micro- and nanostructured thin films. *J. Vac. Sci. Technol., A* **2007**, *25*, 1317–1335.

(47) Martinu, L.; Poitras, D. Plasma deposition of optical films and coatings: A review. *J. Vac. Sci. Technol., A* **2000**, *18*, 2619–2645.

(48) Badorreck, H.; Steinecke, M.; Jensen, L.; Ristau, D.; Jupé, M.; Müller, J.; Tonneau, R.; Moskovkin, P.; Lucas, S.; Pflug, A.; et al. Correlation of structural and optical properties using virtual materials analysis. *Opt. Express* **2019**, *27*, 22209–22225.

(49) Badorreck, H.; Jensen, L.; Ristau, D.; Jupé, M. Statistical Analysis on the Structural Size of Simulated Thin Film Growth with Molecular Dynamics for Glancing Angle Incidence Deposition. *Coatings* **2021**, *11*, 469.

(50) Grineviciute, L.; Badorreck, H.; Jensen, L.; Ristau, D.; Jupé, M.; Selskis, A.; Tolenis, T. Impact of deposition conditions on nanostructured anisotropic silica thin films in multilayer interference coatings. *Appl. Surf. Sci.* **2021**, *562*, 150167.

(51) Herzbach, D.; Binder, K.; Müser, M. H. Comparison of model potentials for molecular-dynamics simulations of silica. *J. Chem. Phys.* **2005**, *123*, 124711.

(52) Paramore, S.; Cheng, L.; Berne, B. J. A Systematic Comparison of Pairwise and Many-Body Silica Potentials. *J. Chem. Theory Comput.* **2008**, *4*, 1698–1708.

(53) Combariza, A. F.; Gomez, D. A.; Sastre, G. Simulating the properties of small pore silica zeolites using interatomic potentials. *Chem. Soc. Rev.* **2013**, *42*, 114–127.

(54) Cowen, B. J.; El-Genk, M. S. On force fields for molecular dynamics simulations of crystalline silica. *Comput. Mater. Sci.* **2015**, *107*, 88–101.

(55) Pedone, A.; Bertani, M.; Brugnoli, L.; Pallini, A. Interatomic potentials for oxide glasses: Past, present, and future. *J. Non-Cryst. Solids* **2022**, *15*, 100115.

(56) Mortier, W. J.; Ghosh, S. K.; Shankar, S. Electronegativity-equalization method for the calculation of atomic charges in molecules. *J. Am. Chem. Soc.* **1986**, *108*, 4315–4320.

(57) Chenoweth, K.; van Duin, A. C. T.; Goddard, W. A. ReaxFF Reactive Force Field for Molecular Dynamics Simulations of Hydrocarbon Oxidation. *J. Phys. Chem. A* **2008**, *112*, 1040–1053.

(58) Yu, Y.; Wang, B.; Wang, M.; Sant, G.; Bauchy, M. Revisiting silica with ReaxFF: Towards improved predictions of glass structure and properties via reactive molecular dynamics. *J. Non-Cryst. Solids* **2016**, *443*, 148–154.

(59) Shchygol, G.; Yakovlev, A.; Trnka, T.; van Duin, A. C. T.; Verstraelen, T. ReaxFF Parameter Optimization with Monte-Carlo and Evolutionary Algorithms: Guidelines and Insights. *J. Chem. Theory Comput.* **2019**, *15*, 6799–6812.

(60) van Duin, A. C. T.; Strachan, A.; Stewman, S.; Zhang, Q.; Xu, X.; Goddard, W. A. ReaxFFSiO Reactive Force Field for Silicon and Silicon Oxide Systems. *J. Phys. Chem. A* **2003**, *107*, 3803–3811.

(61) Defoort-Levkov, G. R. N.; Bahm, A.; Philipp, P. Influence of water contamination on the sputtering of silicon with low-energy argon ions investigated by molecular dynamics simulations. *Beilstein J. Nanotechnol.* **2022**, *13*, 986–1003.

(62) Defoort-Levkov, G. R. N.; Bahm, A.; Philipp, P. Ultralow-energy amorphization of contaminated silicon samples investigated by molecular dynamics. *Beilstein J. Nanotechnol.* **2023**, *14*, 834–849.

(63) Zhang, X.; Duan, Y.; Dai, X.; Li, T.; Xia, Y.; Zheng, P.; Li, H.; Jiang, Y. Atomistic origin of amorphous-structure-promoted oxidation of silicon. *Appl. Surf. Sci.* **2020**, *504*, 144437.

(64) Capaldi, L.; Sansoz, F. High-temperature active oxidation of nanocrystalline silicon-carbide: A reactive force-field molecular dynamics study. *Acta Mater.* **2023**, *258*, 119229.

(65) Moqadam, M.; Riccardi, E.; Trinh, T. T.; Åstrand, P.-O.; van Erp, T. S. A test on reactive force fields for the study of silica dimerization reactions. *J. Chem. Phys.* **2015**, *143*, 184113.

(66) Pitman, M. C.; van Duin, A. C. T. Dynamics of Confined Reactive Water in Smectite Clay–Zeolite Composites. *J. Am. Chem. Soc.* **2012**, *134*, 3042–3053.

(67) Fogarty, J. C.; Aktulga, H. M.; Grama, A. Y.; van Duin, A. C. T.; Pandit, S. A. A reactive molecular dynamics simulation of the silica-water interface. *J. Chem. Phys.* **2010**, *132*, 174704.

(68) Plimpton, S. Fast parallel algorithms for short-range molecular dynamics. *J. Comput. Phys.* **1995**, *117*, 1–19.

(69) Willems, T. F.; Rycroft, C. H.; Kazi, M.; Meza, J. C.; Haranczyk, M. Algorithms and tools for high-throughput geometry-based analysis of crystalline porous materials. *Microporous Mesoporous Mater.* **2012**, *149*, 134–141.

(70) Stukowski, A. Visualization and analysis of atomistic simulation data with OVITO—the Open Visualization Tool. *Modell. Simul. Mater. Sci. Eng.* **2010**, *18*, 015012.

(71) Mukhopadhyay, A. B.; Oligschleger, C.; Dolg, M. Molecular dynamics investigation of structural properties of a zeolite ZSM-5 based amorphous material. *Phys. Rev. B* **2003**, *67*, 014106.

(72) Dijkstra, E. W. A note on two problems in connexion with graphs. *Numer. Math.* **1959**, *1*, 269–271.

#### ■ NOTE ADDED AFTER ASAP PUBLICATION

This paper was published ASAP on September 30, 2024 with an error in the caption of Figure 5. The corrected version reposted October 1, 2024.